Far-infrared bandpass filters from cross-shaped grids

V. P. Tomaselli, D. C. Edewaard, P. Gillan, and K. D. Möller

The optical transmission characteristics of electroformed metal grids with inductive and capacitive cross patterns have been investigated in the far-infrared spectral region. The transmission characteristics of one- and two-grid devices are represented by transmission line theory parameters. Results are used to suggest construction guidelines for two-grid bandpass filters.

I. Introduction

Far-infrared bandpass and bandstop filters made from inductive or capacitive crosses have been reported by Ulrich.[1] The cross grids used to generate the various patterns for the filters are fabricated by a photoetching process. For example, a mask may be made by combining (that is, overlaying) a simple capacitive and inductive grid. The resulting pattern may itself be used as an original to generate additional capacitive as well as inductive crosses. The transparent regions of these cross grids, while not exactly symmetric, can be enlarged during the photoetching process. Thus, different crosses and variations of the patterns may be produced using this method.

Interest in such bandpass filters arose in the planning of NASA's diffuse infrared background experiment (DIRBE) which is to be carried aloft aboard the Cosmic Background Explorer (COBE) satellite.[2] For measurements in the 30–50- and 50–80-cm^{-1} regions required in this experiment, such far-infrared bandpass filters are desirable.

Our interest is to study in detail the transmission characteristics of such bandpass filters in the passband region. The stopband region is not of interest here since all unwanted radiation will be eliminated by the use of the detectors selected and available low pass filters.[3] In addition, the results of transmission line theory, as formulated by Ulrich,[4] may only be applied to the long wavelength or passband region.

The authors are with Fairleigh Dickinson University, Physics Department, Teaneck, New Jersey 07666.

Received 3 October 1980.
0003-6935/81/081361-06$00.50/0.

II. Production of Meshes

An inductive cross pattern is one that has the cross interior transparent while the surrounding region is opaque (see Fig. 1). Capacitive meshes are the negative of inductive meshes. Grids with inductive crosses were produced using a method very similar to the procedure described by Ulrich.[5] A 2.5-μm thick Mylar substrate was stretched and glued on a metal ring and then coated (vacuum deposited) with copper. The copper layer was coated with Kodak Ortho Resist type 3 thinned with the appropriate thinner in a 1:1 ratio. After a portion of the copper layer was covered with the photoresist solution, an even distribution of the photoresist was achieved by spinning the substrate. The substrate was then baked for 30 min at 60°C. The latent grid image was produced by covering the photoresist layer with a mask and exposing it to light from a 100-W mercury vapor lamp at a distance of ~1 m for 40 sec. The filter was developed for 40 sec in Kodak Ortho Resist developer, dried by spinning for 20–30 sec, and again baked for 3 min at 60°C.

The mask for the exposure process was made by superimposing an inductive and a capacitive grid. Such a mask has transparent crosses, the negative of which will result in opaque crosses. The negative image was used as the mask. Using negative photoresist, the developed filter has unprotected copper crosses which can be etched out using a solution of ferric chloride (50-g $FeCl_3 \cdot 5H_2O$ per liter of water). The size of the crosses can be controlled somewhat by varying the etching time. Figure 2 contains 100× enlargements of crosses produced using two grids with mesh sizes of 280 and one of 150 (a 280 mesh has 280 lines/in.). For the study reported here no attempt has been made to determine the thickness of the copper layer.

III. Measurements on Single Grids

The transmission characteristics of the inductive cross grids, Fig. 1(a), were studied using a Fourier transform spectrometer similar to the one described by Bottema and Bolle.[6] The interferometer has two con-

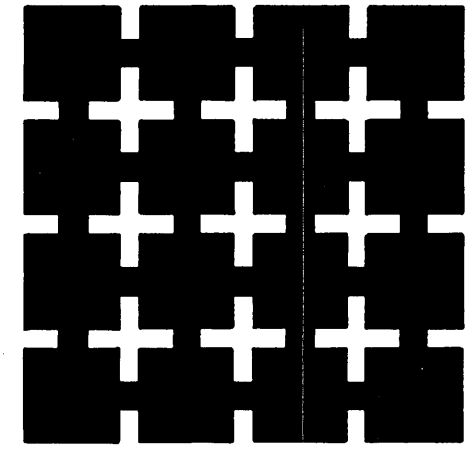

(a)

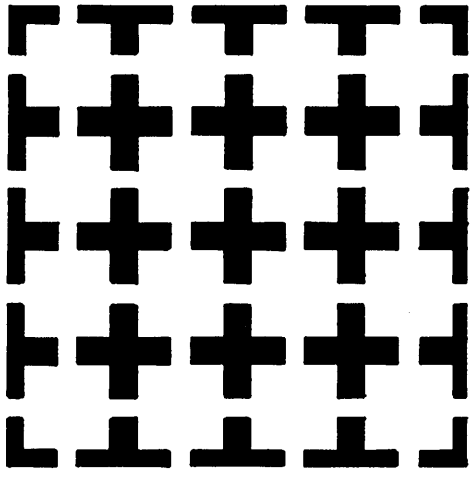

(b)

Fig. 1. (a) Inductive and (b) capacitive cross grid pattern. Black areas are metallic, i.e., deposited copper.

cave mirrors in the arms and a beam splitter. A 250-W mercury vapor lamp provides radiation, by way of a third concave mirror, at the entrance aperture. The exit aperture is the larger opening of a light cone, while the Golay detector is placed at the smaller opening. One of the concave mirrors is translated using a stepping motor. Under low resolution conditions, we have observed only symmetrical interferograms over the total path of the mirror on both sides of the interference maxima. The interferometer is enclosed in a vacuum-tight tank. Samples are positioned in front of the larger opening of the light cone. Test spectra on samples having known transmission characteristics confirmed the good performance of the instrument.

The transmission spectra of the 280, 250, 200, and 150 grids are shown in Figs. 3 and 4. Curve labeling schemes are explained in the figure captions.

IV. Theoretical Representation of Transmission Curves

Simple capacitive or inductive grids, which have resonant frequencies given by $\nu_R \simeq g^{-1}$ where g is the grid constant (reciprocal of mesh number), may be used

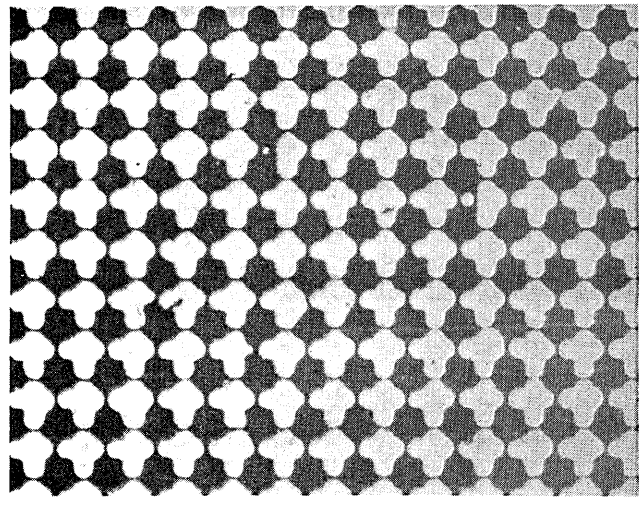

(a)

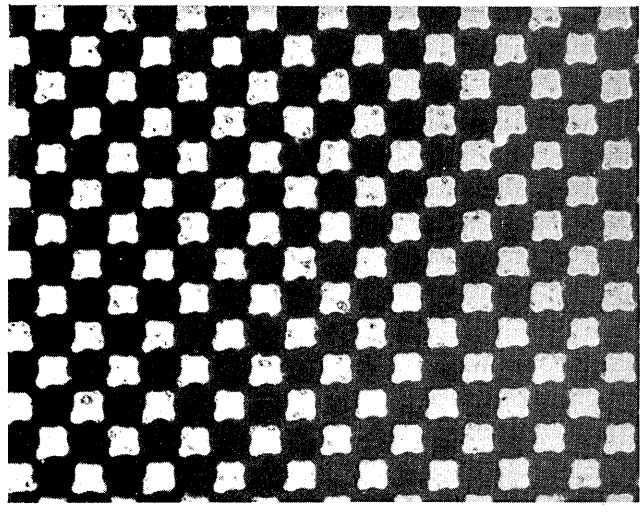

(b)

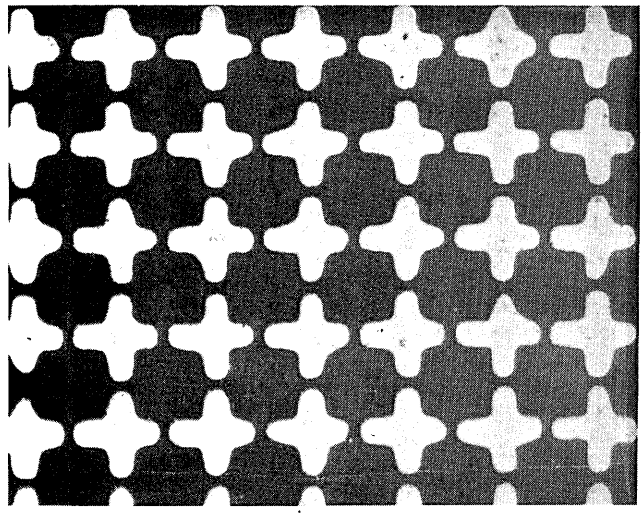

(c)

Fig. 2. Microphotographs of etched cross grids: (a) and (b) are 280 lines/in. and (c) is 150 lines/in.

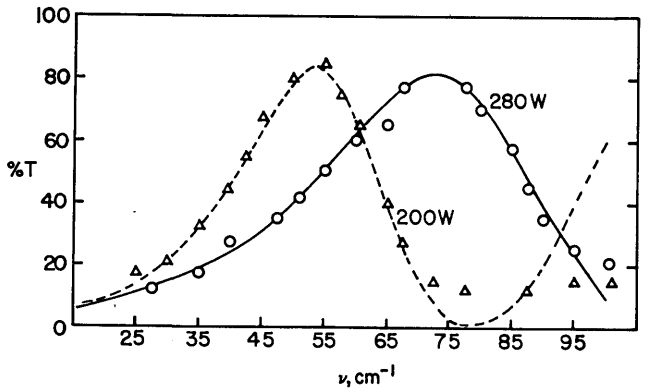

Fig. 3. Measured transmission of single inductive cross grid. Points are experimental; lines present theoretical fits. Parameters used to calculate the theoretical fit are given in Table I. For the 200-W cross grid, theoretical values above 70 cm^{-1} should be disregarded (see text).

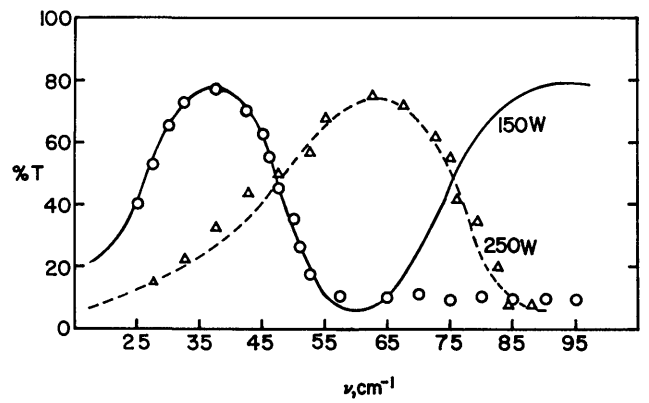

Fig. 4. Measured transmission of single inductive cross grid. Points are experimental; lines present theoretical fits. Parameters are given in Table I. For the 150-W cross grid, theoretical values above 70 cm^{-1} should be disregarded (see text).

in a Fabry-Perot interferometer. They may be mounted such that the spacing between grids corresponds to a first-order resonance. In contrast, inductive cross grids are already resonant. That is, they correspond in an analogous way to two simple grids used at the resonant spacing. However, these cross grids have a lower resonant frequency given by $\nu_R \simeq 0.5\, g^{-1}$. This value of ν_R is below the diffraction region. The product $\nu_R \cdot g$ = constant obviously will depend on geometric parameters such as the ratio a/g (where $2a$ is the width of the wire forming the grid) for an ideal or perfect grid reproduction. Thus, it is a useful quantity to characterize the grid. It was found that variation of the geometry of the opaque areas, for example, due to excessive etching, affects the value of this constant.

The experimental transmission data, as in Figs. 3 and 4, may be represented using transmission line theory as developed by Ulrich.[4] The notation used is that of Ref. 7. Our inductive cross grid was produced by using a superposition of an inductive and a capacitive grid (of

Table I. Parameters Used to Fit Transmission Line Theory to Measured Transmission of Single Inductive Cross Grids

Mesh	Ξ_c	Ξ_i	$\overline{R}_c$	$\overline{R}_i$
280	1.60	1.38	0.015	0.25
250B	1.45	1.37	0.06	0.25
200	1.80	1.17	0.045	0.015
150	1.68	1.73	0.04	0.35

equal periodicities) to form the master mask. The general equivalent circuit for a grid is that of a four-terminal transmission line with a lumped admittance. Therefore, as a starting point for the representation, we write for the admittance of the two cross grids

$$Y = \frac{2}{\overline{R}_c + j\Omega\,\Xi_c} + \frac{2}{\overline{R}_i - j\dfrac{\Xi_i}{\Omega}}, \tag{1}$$

where Ξ_c and Ξ_i are, respectively, the impedances of the capacitive and inductive grids at the resonant frequency ω_0, and

$$\Omega = \frac{\omega}{\omega_0} - \frac{\omega_0}{\omega} \tag{2}$$

is the generalized frequency. Also, $\overline{R}_c$ and $\overline{R}_i$ are the resistances of the grids. The admittance as well as impedance have been normalized to unity.

In Figs. 3 and 4, the solid lines represent the fitted transmission curves. Table I contains the values of the parameters used. Small variations in ω_0 were found to be insignificant, and we have set $\omega_0 = 1$. The theory is only useful below the diffraction region.[4] Therefore, for the higher frequency region in all our investigations, the theoretical curves should be disregarded.

For truly complementary inductive and capacitive grids, the resonance frequency ω_0 and the impedances Ξ_i and Ξ_c can be expressed in terms of a/g. They are also related by the product $\Xi_i\,\Xi_c = K$ = constant. For the ideal case, that is, complementary grids, $K = 1/4$. For irregular or enlarged grid patterns, the value of K will vary. In addition, the resistances $\overline{R}_i$ and $\overline{R}_c$ are expressible in terms of a/g as well as other parameters. Therefore, for complementary grids, the admittance in Eq. (1) depends upon a/g and the parameters contained in the resistance terms.

The photoetching process results in a cross grid which is not composed of precisely complementary capacitive and inductive grid patterns. In the photolithographic process, the transparent crosses may be enlarged and deformed by extended etching times (see Fig. 2). The inductive property, that is, the width of the metallic bridges connecting the opaque squares, corresponds to the important characterization of these grids. This is because their inductive property dominates their capacitive one.

We have determined the representative parameters of 280-line/in. grids with two widely different cross openings [Figs. 2(a) and (b)]. Also, the transmission curve for a third set of parameters giving an inductive impedance between those of the first two crosses has been calculated. The parameters are given in Table II,

Table II. Parameters Used to Calculate Transmission Curves in Fig. 5

Cross Mesh	Ξ_c	Ξ_i	$\overline{R}_c$	$\overline{R}_i$
280B	1.70	0.88	0.15	0.400
280W calc.	1.65	1.33	0.25	0.475
280A	1.60	2.12	0.35	0.550

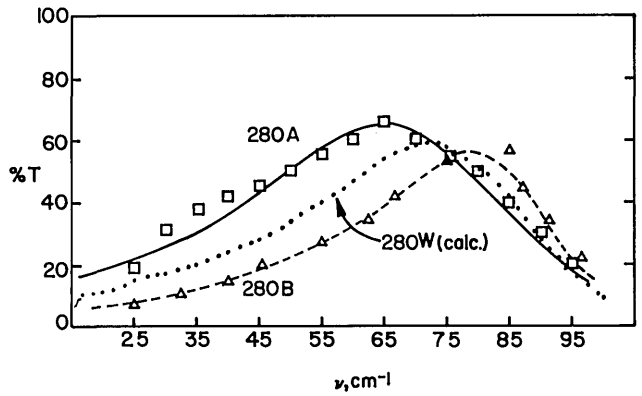

Fig. 5. Transmission of 280-lines/in. inductive grids. See Fig. 2 for photographs of 280 A and 280 B. Points are experimental; lines are theoretical fits. Parameters are given in Table II. The calculated transmission curve, labeled as 280 W (calc.), was generated using parameters chosen to lie between the values used for the 280 A and 280 B in Table II.

and these transmission curves are displayed in Fig. 5. From Table II we see that, as the transparent portion of the mesh increases, the value of Ξ_i increases, an effect observed in inductive grids.[4] From Fig. 5 we see that accompanying the increase in Ξ_i is a shift of the peak transmission to longer wavelengths and an increase in the passband width. Both resistances also increase in this direction. We also see a slightly increased peak transmission at the longer wavelength. The capacitive impedances, however, remain almost unchanged. It is possible to find a relationship between Ξ_i and Ξ_c and $\overline{R}_i$ and $\overline{R}_c$ which depends upon the geometry of the etched cross patterns. Such a relationship would reduce the dependence of the transmission characteristics to only two parameters. This has not been pursued here.

V. Capacitive Grid

By treating an inductive cross grid as a master or mask, the corresponding complementary capacitive grid may be photolithographed. Measured transmission curves for 150, 200, and 280 mesh capacitive grids are given in Fig. 6. The width of the resonance curve depends on the geometrical dimensions of the opaque metallic crosses. Both an increase in the width of the wire in the grid pattern and deformation from perfect cross shape broadens the transmission curve.

The solid curves in Fig. 6 represent calculated transmission values obtained from the reciprocal of admittance as given in Eq. (1). This approach seems to be a satisfactory starting point for truly complementary capacitive and inductive cross meshes, where the product of the respective admittances is a constant. The values of the parameters used are given in Table III.

Table III. Parameters Used to Fit Transmission Line Theory to Measured Transmission of Single Capacitive Cross Grids (Plotted in Fig. 6)

Mesh	Ξ_c	Ξ_i	$\overline{R}_c$	$\overline{R}_i$
150M	1.10	1.36	0.001	0.01
200M	0.90	1.22	0.005	0.05
280M	1.43	1.39	0.001	0.01

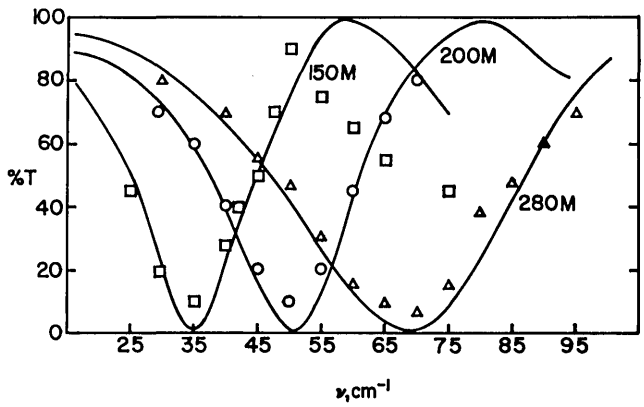

Fig. 6. Transmission of capacitive cross grids. Points are experimental; curves are theoretical. Parameters are given in Table III.

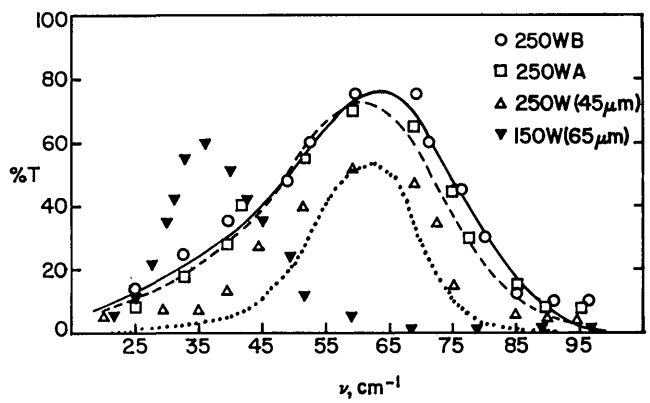

Fig. 7. Experimental (points) and theoretical (lines) transmission of 250- and 150-lines/in. inductive cross grids. Open circles and squares are individual 250 mesh crosses. Open triangles represent a two-grid filter composed of grids A and B separated by 45 μm. Solid inverted triangles represent a 150 mesh pair separated by 65 μm.

VI. Two-Grid Filters

It is interesting to consider the filtering characteristics of a device composed of two grids separated by a given distance. We have investigated such a device and present the results of our measurements in Fig. 7. The two-grid filter was constructed from 250 mesh inductive cross grids. The mesh designated as 250WB was pre-

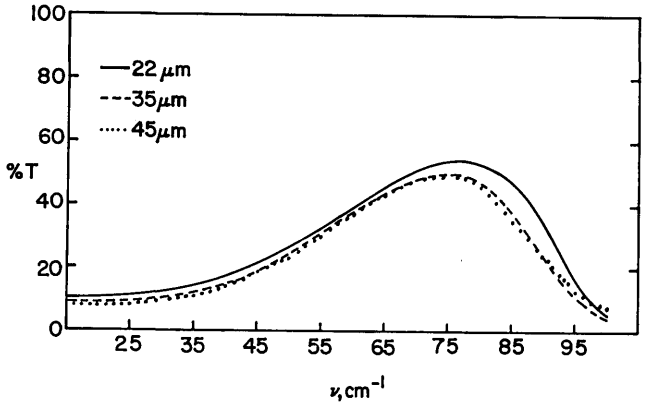

Fig. 8. Calculated transmission of two 280-lines/in. inductive cross grids for three separation distances. Parameters for the individual grids are the same.

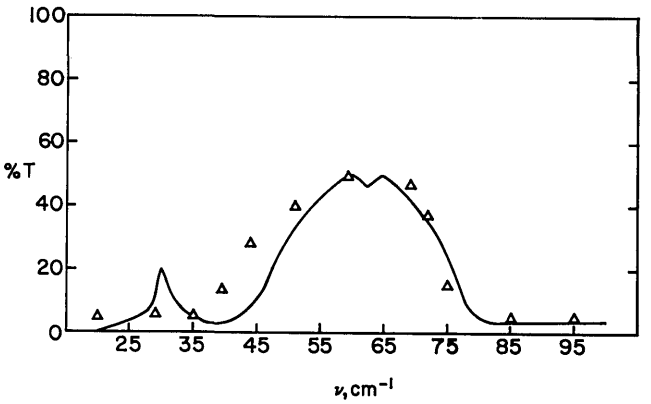

Fig. 9. Measured transmission of two 250-line/in. inductive cross grids separated by 50 μm. Data points are our results; the solid line represents data obtained at higher resolution by J. Heaney (NASA Goddard).

Table IV. Peak Transmission (%) of Two Inductive Cross Grid Filters with Various Separations

S,μm	150 mesh	250 mesh	280 mesh
12	—	32	49 ←[a]
22.5	49	40	50
35	54	50 ←	43
45	56	55	41
57	—	45	41
65	62 ←	—	—
5–7 mm	64	53	45
Transmission of individual grids	78/72	74/78	78/66
Transmission of the product of two grids	56	58	51

[a] Arrows indicate positions corresponding to devices with grid spacings of $\lambda_R/4$.

viously discussed (see Fig. 4). As usual, in Fig. 7 the solid curves represent the calculated fit. The parameters used for the calculated fit of the individual 250 mesh inductive cross grids were also used to generate the calculated transmission curve for the two-grid devices. A grid separation distance of $s = 45$ μm was used. Formulas for the two-grid filters are given by Ulrich *et al.*[8] and need not be reproduced here. The experimental values obtained agree quite well with the calculated curve.

For comparison, the filtering characteristics of a device composed of two 150 mesh inductive cross grids separated by a distance of $s = 65$ μm are also shown in Fig. 7. For this device, the peak transmission is shifted to longer wavelengths and increases to over 60%.

A single cross grid is, as pointed out by Ulrich,[1] distinctly different from either a single-capacitive or single-inductive grid having a simple square symmetry. Two capacitive or two inductive grids may be assembled to form a Fabry–Perot device, which, for appropriate grid separations, exhibits a resonance behavior. However, the single cross grid itself exhibits resonance behavior. Combining two cross grids should yield a filter having a maximum transmission at grid separations of $\lambda_R/4$, where λ_R is the wavelength corresponding to the peak transmission of a single cross grid. In Fig. 8 we show the results of a theoretical study of the effect of grid separation on the transmission of a filter made from two 280 mesh inductive crosses. The grid separations used were 22, 35, and 45 μm. Table IV presents values of the peak transmission of such devices as determined from measurements on a number of filters composed of 150, 250, and 280 mesh inductive crosses. The arrows found in Table IV represent the positions where devices with grid spacings of $\lambda_R/4$ would be found. It can be seen from both Table IV and Fig. 8 that the highest transmissions are indeed found for grid spacings near $\lambda_R/4$. The experimental uncertainty in this work is, however, ~5%. Table IV shows that the transmission of these two grid filters does not appreciably change for large grid separations, for example, 5–7 mm, and that the transmission is essentially given by the product of the single-grid values.

In Fig. 9 we show transmission data for a two 250 mesh inductive cross filter. The solid line shows data obtained by J. Heaney at NASA Goddard Space Flight Center using a Nicolet instrument with a liquid helium cooled detector. The secondary transmission maxima at ~30 cm^{-1} was also observed by us for some two-grid filters. Because this secondary maximum was not always observed it was speculated, initially, that it was spurious and was attributed to division of small numbers at these low frequencies. However, such low frequency side maxima have been reported by Ulrich[1] on a four-layer filter made from inductive crosses. Transmission line theory, as used here, does not allow for such a low frequency peak. Other calculational methods for treating reflection from an inductive cross pattern, such as that given by Agrawal and Imbriale,[9] are available and, if properly applied, may explain this observation.

From the point of view of filter design, our primary interest in undertaking the project, we would like to offer some concluding remarks. (1) It appears from Fig. 5 that as one enlarges the transparent regions of a single mesh inductive cross grid, for example, by excessive etching of the metallic crosses, that the transmission peak shifts to longer wavelengths, increases in height, and broadens in the bandpasses. (2) Considering Fig. 2, one is led to visualize a checkerboard pattern [Fig. 2(b)] as the inductive crosses are progressively etched. We have made a preliminary study of such a checkerboardlike pattern. By carefully controlling the photoetching process, it is possible to vary widely the transparent region while preserving the metallic bridges between squares. Initial measurements on these single mesh filters have shown good transmission properties. A recent paper by Davis[10] also describes studies of such a structure but does not include the observation of the low frequency side peak mentioned above. (3) From Fig. 7 and Table IV it appears that the distance between the two grids in a two-layer filter is not a very important factor. This implies a construction method ideally suited to satellite use. That is, one produces the desired grid patterns on both sides of a quartz window. With a window thickness suitably chosen, to avoid interference fringes, a rugged easy-to-mount filter can be fabricated.

Parts of this work were supported by NASA contract NAS5-25483 and by the U.S. Army ARRADCOM contract DAAG 29-79-C-0130.

We would like to thank J. Heaney of the NASA Goddard Space Flight Center for interesting discussions and the reported measurements.

References

1. R. Ulrich, Appl. Opt. **7**, 1987 (1968).
2. See, for example, J. Mather, Astronaut. Aeronaut. **16**, 60 (1978).
3. S. P. Varma and K. D. Möller, Appl. Opt. **8**, 1663 (1969).
4. R. Ulrich, Infrared Phys. **7**, 37 (1967).
5. R. Ulrich, Appl. Opt. **8**, 319 (1969).
6. M. Bottema and H. J. Bolle, paper presented at Aspen International Conference on Fourier Spectroscopy (1970), contribution 19.
7. K. D. Möller and W. G. Rothchild, *Far-Infrared Spectroscopy* (Wiley-Interscience, New York, 1971), Chap. 3.
8. R. Ulrich, T. J. Bridges, and M. A. Pollack, Appl. Opt. **9**, 2511 (1970).
9. V. D. Agrawal and W. A. Imbriale IEEE Trans. Antennas Propag. **AP-27**, 466 (1979).
10. J. E. Davis, Infrared Phys. **20**, 287 (1980).

Books *continued from page 1360*

elucidation of a more general conceptual base. Specifically, there is the development of the notion that understanding charged-particle collision processes and their unique characteristics in electric and magnetic fields forms the truly unique aspect of the physics of plasmas. Indeed, this book is written for the student and researcher with a background in physics; it would thus also be valuable to those readers with an engineering background because of the detailed factual material as well as the approach that is taken.

Based on a course of lectures given to undergraduate and graduate students, the sequential development of ideas serves to define unique aspects of plasma behavior by relating them to well-understood neutral gas physics. The introduction includes a definition of time and length scales related to electric fields, but the authors choose to ignore magnetic fields. This marks the initiation of a unique (and cumbersome to this reviewer) approach to the study of plasmas. Specifically, charged particles in magnetic fields are first discussed in detail in Chap. 8 (p. 241). This technique of considering electric field effects as primary could prove to be effective in simplifying the learning process, but it simultaneously places consideration of magnetic field effects on charged particles in a position of secondary importance. There are some problems: magnetic field effects are included without comment in a Boltzmann equation (Chap. 3), in the alteration of the electron distribution functions (Chap. 5), and in the equations for momentum and heat flux (Chap. 6). The experienced reader and teacher can adjust to this approach, but it is a unique characteristic of the book. There is limited discussion of device-oriented material, but this does not present a problem. In fact, there is some excellent material included which is specifically related to important device physics, e.g., banana orbits in tokamaks (Chap. 8), and MHD instabilities in tokamak geometries (Chap. 9).

With reference to other detailed aspects of the material presented, the description of the classical and quantum mechanical limits on particle collisions (Chap. 2) is clear and useful. It is a bit puzzling why no identification is made of the collisionless Boltzmann equation with the name or work of Vlasov (Chap. 3). The inclusion of directed velocities with the distribution function development is appreciated (Chap. 4). Likewise the time given to perturbations of the Maxwellian distribution is well spent. The moment equations are then developed to describe transport in weakly and strongly ionized gases, and the treatment is thorough and comprehensive.

This book will provide a truly unique reference for those students and research workers in plasma diagnostics, plasma transport, and laser–plasma interactions. Thorough coverage of all the important plasma physics parameters are presented with a consistency and compatability not frequently evident in basic plasma references.

T. M. YORK

Solar Flares. Edited by PETER A. STURROCK. Colorado Associated University Press, Boulder, 1980. 513 pp. $17.50.

Skylab provided an array of solar instruments enabling teams of astronauts to study the sun over a period of 171 days. The six major instruments were: (a) a white-light coronograph yielding some 3500 photographs and covering over 100 transient eruptions; (2) an x-ray spectrographic telescope yielding 32,000 photographs; (3) an x-ray telescope giving 28,000 images over the range 3 to 53 Å; (4) a UV spectrometer–spectroheliometer providing information in the range 280 to 1350 Å and making continuous measurements of seven selected lines spanning the temperature range 10^4 to $10^{6.3}$ K; (5) an extreme UV spectroheliograph working in the range 171 to 630 Å; and (6) an UV spectrograph covering the range 970 to 394 Å. The spatial resolution of the major instruments ranged from 2 to 10 sec of arc. The supporting instruments included two Hα telescopes, an XUV monitor, an x-ray event analyzer, a photomultiplier exposure counter, and a 6-cm band radio monitor.

A series of workshops was established to study the wealth of information returned to earth, together with supporting ground based data. The second of these workshops was concerned with solar flares. Seven teams were formed concerned, respectively, with (1) the preflare state—multithermal flare structure, forerunners of coronal transients and the preflare magnetic field geometry, (2) primary energy release, (3) energetic particles—abundances, acceleration, and reverse currents, (4) the impulsive phase—x-ray spectra, x-ray source location and beaming, time variation of hard x-ray emission, (5) the chromosphere and the transition region, (6) mass ejection, and (7) thermal x-ray emitting plasma. This monograph presents the results

continued on page 1373